ARTICLE OPEN

Check for updates

Evolution of electronic and magnetic properties of Sr_2IrO_4 under strain

Ekaterina M. Pärschke[1]✉, Wei-Chih Chen[2], Rajyavardhan Ray[3,4,5] and Cheng-Chien Chen[2]

Motivated by properties-controlling potential of the strain, we investigate strain dependence of structure, electronic, and magnetic properties of Sr_2IrO_4 using complementary theoretical tools: ab-initio calculations, analytical approaches (rigid octahedra picture, Slater-Koster integrals), and extended $t-\mathcal{J}$ model. We find that strain affects both Ir-Ir distance and Ir-O-Ir angle, and the rigid octahedra picture is not relevant. Second, we find fundamentally different behavior for compressive and tensile strain. One remarkable feature is the formation of two subsets of bond- and orbital-dependent carriers, a compass-like model, under compression. This originates from the strain-induced renormalization of the Ir-O-Ir superexchange and O on-site energy. We also show that under compressive (tensile) strain, Fermi surface becomes highly dispersive (relatively flat). Already at a tensile strain of 1.5%, we observe spectral weight redistribution, with the low-energy band acquiring almost purely singlet character. These results can be directly compared with future experiments.

npj Quantum Materials (2022)7:90; https://doi.org/10.1038/s41535-022-00496-w

INTRODUCTION

Exploring the physics of quasi-two-dimensional (2D) spin-orbit Mott insulators can help to understand high-temperature superconductivity as well as the general interplay of spin-orbit coupling, Hund's, and Coulomb interactions. In particular, a lot of studies have been devoted to the quasi-2D iridates Sr_2IrO_4 and Ba_2IrO_4[1–3]. Iridates show eminent similarities to the cuprate family of high-temperature superconductors, both in structure and low-energy physics, and were expected to become superconducting upon doping. However, so far no superconductivity has been reported in iridates.

In general, Sr_2IrO_4 behavior often deviates from theoretical predictions. For example, Mott insulators normally become metallic at high enough pressure as the unit cell becomes smaller and the bands broaden. This is also true for spin-orbit coupled Mott insulators, such as ruthenates[3,4]. In Sr_2IrO_4, resistance indeed decreases until the pressure of around 25–30 GPa (which according to ref. [5], corresponds approximately to a strain of −4%)[5], or, according to a very recent study[6], 32–38 GPa (−5.1% strain). Then, however, resistance starts to increase, showing a peculiar U-shaped dependency and persisting insulating behavior up to at least 185 GPa[6]. So far, no metallization in Sr_2IrO_4 or other iridates ($Sr_3Ir_2O_7$[7,8], $BaIrO_3$[3,9], etc) has been observed at pressures up to 40–185 GPa[3,6]. Moreover, there is also surprisingly little correlation between the insulating behavior and magnetism[10] as the latter disappears at around 20 GPa (roughly −2.9% strain) in Sr_2IrO_4[5,11] and 14.4 GPa (roughly −2.1% strain) in $Sr_3Ir_2O_7$[8], without the onset of a metal-insulator transition.

Furthermore, iridates emerge as a good functional playground for manipulation of the magnetic and electronic properties, which is an exciting goal both fundamentally and practically[3,12]. Iridium-based heterostructures and superlattices have therefore emerged as a whole new field very recently[13–21]. Strain and pressure in particular are powerful tools on hand to control the magnetic properties of the material. It has been shown that misfit strain can directly control dispersion of magnetic excitations in Sr_2IrO_4[22–24], as well as transport properties[25]. A shift of the two-magnon Raman peak to higher energies was observed under tensile strain[24], albeit much weaker than the shift observed in the canonical Mott–Hubbard insulator K_2NiF_4 and cuprates like $Bi_{1.98}Sr_{2.06}Y_{0.68}Cu_2O_{8+\delta}$[26].

In ref. [23], the authors used resonant inelastic scattering (RIXS) to show that magnetic dispersion in Sr_2IrO_4 is strongly affected by strain. In particular, the contribution of the second and third nearest-neighbor (NN) exchange was suppressed (enhanced) upon tensile (compressive) strain. The tensile strain was shown to drive the system closer to a shorter-range first-NN only Heisenberg limit, with only little magnon branch softening left at $(\pi/2, \pi/2)$ already upon the tensile strain of +2%. Upon compressive strain, the energy of $(\pi, 0)$ magnon was shown to increase[22,23].

A clear understanding of the electronic and magnetic properties of iridates and their evolution with strain is, therefore, of interest not only from a fundamental point of view but also for applications[3,12]. Unveiling the details of the interplay of lattice, magnetic, and other degrees of freedom in Sr_2IrO_4 is needed to understand the recently observed electrical control of octahedra rotation[27,28] and the much-debated strong magnetoelastic coupling[29–32]. Currently, a clear understanding of neither how exactly nor by which mechanism do superexchange and hopping parameters in Sr_2IrO_4 change with strain is available, not even on a phenomenological level. One of the interesting questions is whether the change in electronic and magnetic properties upon the strain is mostly associated with bond length change, as argued in e.g., ref. [22], or the change of the in-plane rotation angles θ of the oxygen octahedra (see Fig. 1)[33].

Studying the behavior of iridates under strain and pressure is a demanding task not only experimentally, but also theoretically. On one hand, iridates are strongly correlated Mott insulators[1], so one needs to resort to theoretical methods where correlations are

[1]Institute of Science and Technology Austria, Am Campus 1, 3400 Klosterneuburg, Austria. [2]Department of Physics, University of Alabama at Birmingham, Birmingham, AL 35294, USA. [3]Leibniz IFW Dresden, Helmholtzstr. 20, 01069 Dresden, Germany. [4]Dresden Center for Computational Material Science (DCMS), TU Dresden, 01062 Dresden, Germany. [5]Department of Physics, Birla Institute of Technology Mesra, Ranchi 835215, India. ✉email: ekaterina.paerschke@ist.ac.at

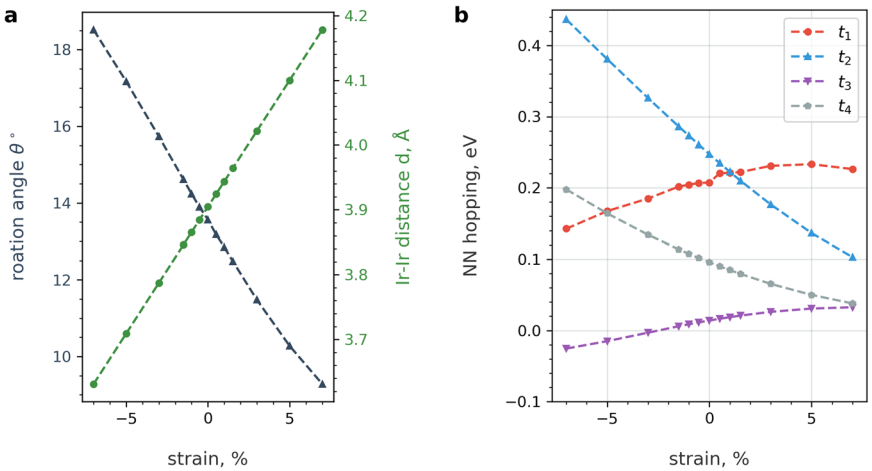

Fig. 1 Dependency of the octahedra rotation angle θ, Ir-Ir distance d, and NN hopping parameters on strain. a The in-plane IrO_6 octahedral rotation angle θ and Ir-Ir distance d as functions of strain, obtained with full structure relaxation in DFT calculations (see Methods). **b** NN hopping parameters for different values of strain, see Fig. 1 for notation.

treated non-perturbatively, employing effective descriptions like Hubbard or Heisenberg models. On the other hand, microscopic changes of orbitals, their overlap, and structural changes are essential to understand the behavior of a crystal under strain[34–38], so ab-initio methods are demanded. Another difficulty is that as one eventually approaches a possible metal–insulator transition at high pressure and/or strain, effective models, such as the Heisenberg superexchange model, fail.

In this paper, we focus on the effect of strain and combine various complementary theoretical tools to provide a comprehensive analysis of how the magnetic properties are affected by strain. For different (compressive and tensile) strain values, we use density functional theory (DFT) based ab-initio calculations to access microscopic changes in the crystal structure, and study the corresponding changes in the electronic properties through Wannierization of the scalar-relativistic DFT bandstructure obtained within the generalized gradient approximation[39]. Subsequently, we solve an extended $t-\mathcal{J}$ model within the self-consistent Bohr approximation (SCBA) to obtain the angle-resolved photoemission spectra (ARPES) and study the strain-controlled evolution of the Fermi surface. Realistic values of the input parameters for these calculations were used: the hopping parameters were obtained from the DFT calculations, while the extended-range exchange couplings were obtained by direct comparison to the magnon dispersion measured with RIXS. In this way, the presented analysis contains no free parameters apart from an overall constant energy shift (chemical potential) in the SCBA calculations.

RESULTS AND DISCUSSION

Evolution of hopping parameters under strain

Sr_2IrO_4 shows an in-plane staggered octahedra rotation characterized by a single parameter: $\measuredangle O-Ir-Ir$ angle denoted by θ in Fig. 1. Under ambient conditions, the octahedral rotation is found to be $\theta \approx 13.6^\circ$ for the relaxed structure, which is close to the reported experimentally value of 11.8°[40]. The epitaxial strain on iridates then affects not only the distance between the Ir atoms but also the Ir-O-Ir bond angle, as can be seen in Fig. 2a. The in-plane octahedra rotation angle θ, obtained using DFT (see Methods for details), monotonically increases (decreases) upon compressive (tensile) strain in the studied range of -7.5% to 7.5%, where negative strains correspond to compression.

To ascertain the influence of structural changes on the electronic properties, we study the evolution of Wannier tight-binding model hoppings derived from DFT (see Methods for details), as a function of strain (Fig. 2b). The notations for the hoppings are shown in Fig. 1: the intraorbital hoppings between xy orbitals along a' or b' axes is denoted as t_1, between $xz(yz)$ along a' (b') axis as t_2, and between $xz(yz)$ along b' (a') as t_3. The interorbital hopping between yz and xz orbitals is denoted as t_4, all other interorbital hoppings are negligible. Further neighbor interorbital hoppings are denoted as t' and are shown in Fig. 1.

Upon compression, direction-dependent hopping parameter t_2 is increasing, but surprisingly, t_1 is decreasing (Fig. 2b). This emerging anisotropy in hopping parameters is interesting, as t_2 hopping describes the propagation of an electron with xz (yz) orbital character along only one axis, a' (b'), whereas t_1 allows an xy electron to hop in both directions. We thus see that upon compressive strain, the system favors the separation of the entire Fermi sea into two Fermi seas with bond-dependent propagation (xz carriers which can only propagate along a', and yz carriers which can only propagate along b') and suppression of the bond-independent and thus truly two-dimensional xy carriers. This compass-model-like[41] propagation is quite unusual and could cause the formation of charge density wave.

Upon tensile strain, t_1 is nearly independent of the strain value and is the dominant hopping, while t_2 decreases steadily (Fig. 2b). Different behavior of t_1 upon compressive and tensile strain reflects the change of Fermi surface topology between compressive and tensile strain.

It is also interesting to note that the smallest hopping parameter t_3, describing the hopping between almost parallel d-orbitals with very small overlap goes to zero around -3%, which corresponds to compression of ~20 GPa, not too far from the value of resistivity minimum under pressure[5,6].

To disentangle the contribution of inter-atomic distance d and the octahedral rotation θ to the hopping parameter trends with strain, we employ the analytical approaches of Glazer and Slater-Koster. The Glazer picture[42] is often used in rigid octahedra approximation whereby the main effect of the modest strain is assumed to be the change of the in-plane rotation angle θ. However, as detailed in Supplementary Fig. 2, the trends obtained within the Glazer picture disagree with the DFT results in Fig. 2b, and even contradict them in rigid octahedra approximation. Therefore, the Glazer picture has limited applicability for iridates, and rigid octahedra approximation is improper.

We then proceed with a more specific orbital-resolved Slater-Koster-integrals-based approach[43,44]. Slater-Koster integrals are hybridization matrix elements E between atomic d-states on neighboring atoms obtained via integrating over relevant

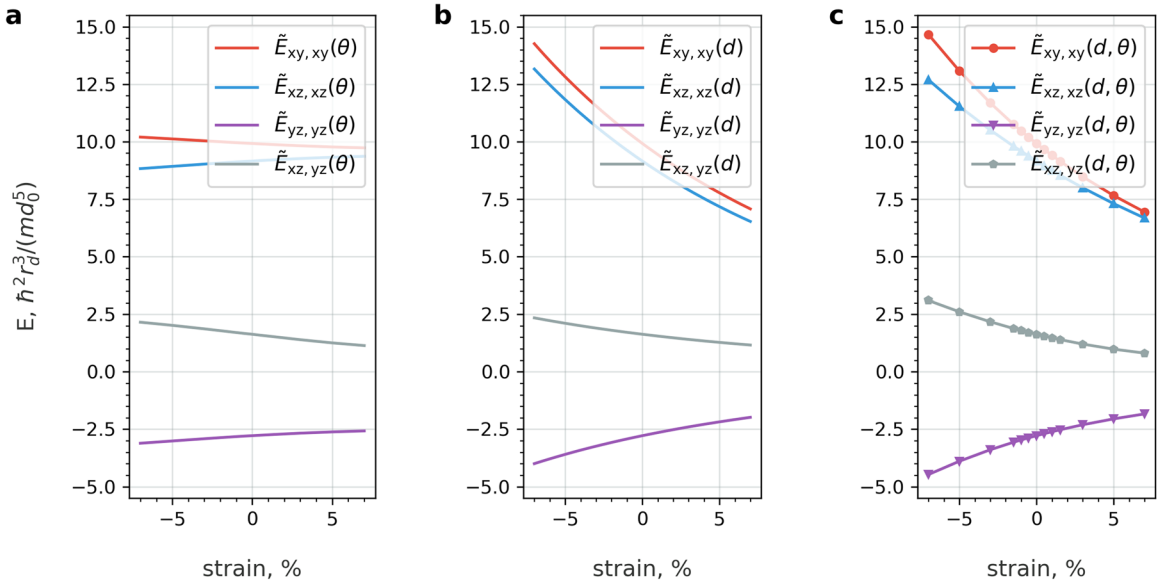

Fig. 2 Dependency of Slater-Koster Ir-Ir integrals on strain. Slater-Koster integrals for rotated NN orbitals $\tilde{E}$ as a function of **a** octahedra in-plane rotation angle θ, **b** Ir-Ir distance d, **c** both θ and d (calculated using values of θ and d extracted from DFT shown in Fig. 2a).

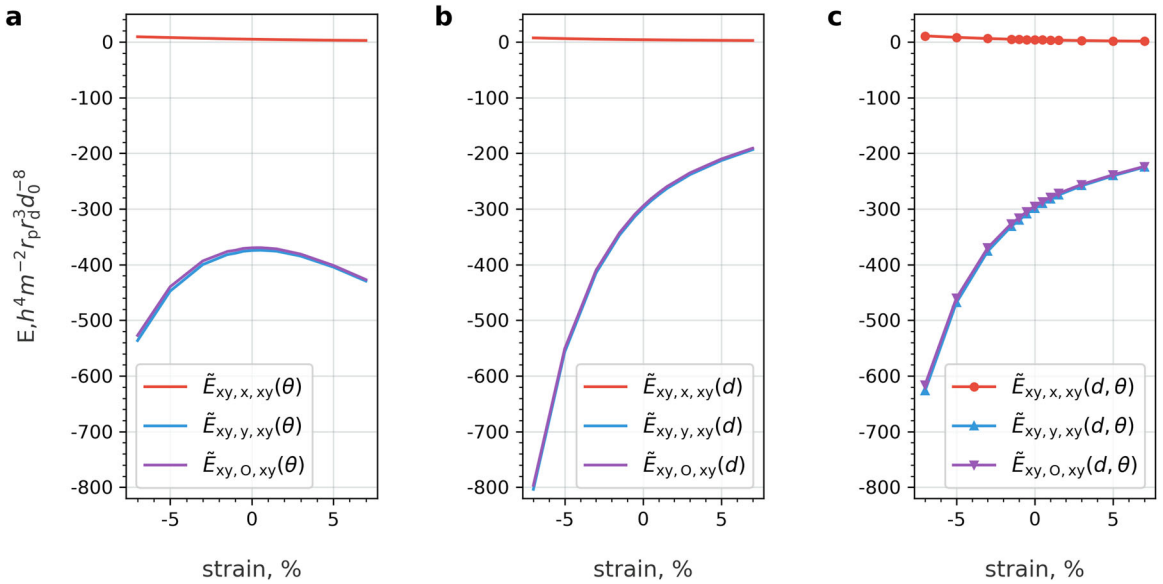

Fig. 3 Dependency of Slater-Koster Ir-O-Ir integrals on the strain. Slater-Koster integrals for indirect hopping between rotated Ir NN orbitals $\tilde{E}$ via oxygen p orbitals as a function of **a** Octahedra in-plane rotation angle θ, **b** Ir-Ir distance d, **c** both θ and d (calculated using values of θ and d extracted from DFT shown in Fig. 2a).

spherical harmonics. The resulting interatomic matrix elements E are proportional to the d-wave functions overlap and can be expressed via cubic harmonic matrix elements $V_{dd\sigma}$, $V_{dd\pi}$, $V_{dd\delta}$ for a known bond direction l, m, n as tabulated in Slater-Koster tables[43,44]. In Sr_2IrO_4, we also need to account for the rotation of the d orbitals within the t_{2g} sector due to the in-plane octahedral rotation[45]. Therefore, we decompose the rotated d orbital on the basis of non-rotated d orbitals before evaluating the Slater-Koster matrix elements. For example, the hybridization matrix element $\tilde{E}$ between the two rotated NN xy orbitals can be obtained as a superposition of hybridization matrix elements E of non-rotated xy and $x{-}y^2$ orbitals obtained as:

$$\tilde{E}_{xy,xy} = \cos^2(2\theta)E_{xy,xy} - \sin^2(2\theta)E_{x^2-y^2,x^2-y^2}, \quad (1)$$

where θ is the in-plane rotation of the IrO_6 octahedra (see Fig. 1). Similarly, for the overlap between the rotated $xz(yz)$ orbitals along the a' direction, we get

$$\tilde{E}_{xz,xz(yz,yz)} = \cos^2(\theta)E_{xz,xz(yz,yz)} - \sin^2(\theta)E_{yz,yz(xz,xz)}, \quad (2)$$

and for interatomic interorbital overlap along x:

$$\tilde{E}_{yz,xz} = E_{yz,xz} + \sin\theta\cos\theta(E_{xz,xz} + E_{yz,yz}). \quad (3)$$

Figure 3 shows the resulting hybridization matrix elements $\tilde{E}$ as a function of the in-plane octahedral rotation θ, the Ir-Ir distance d, as well as both the parameters (see Fig. 2a). We find that at least in the Slater-Koster approximation, accounting for the change of the distance d alone (Fig. 3b) can provide a better approximation to a full dependency of matrix elements $\tilde{E}$ on strain (Fig. 3c) then

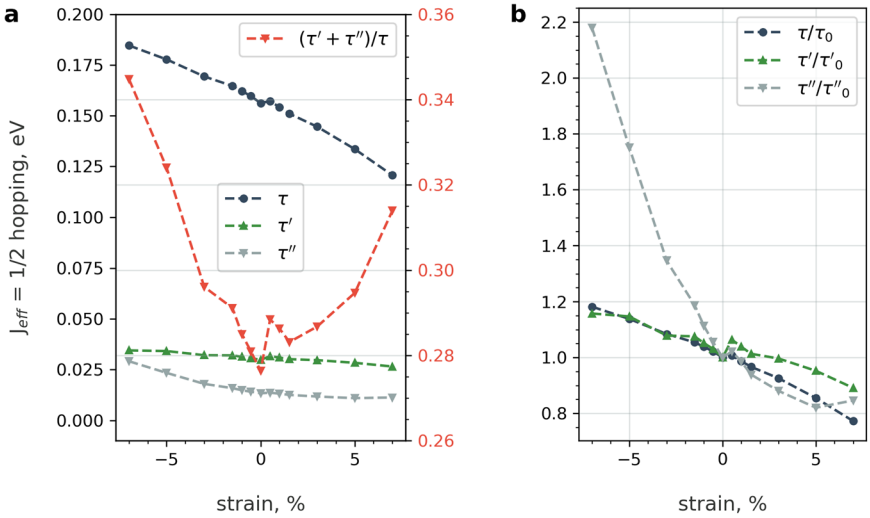

Fig. 4 Dependency of $J_{\mathrm{eff}} = 1/2$ overlap on the strain. a NN, 2NN and 3NN hopping parameters (τ, τ' and τ'', correspondingly) between $J_{\mathrm{eff}} = 1/2$ states calculated as a superposition of obtained from DFT calculations *xy*, *yz*, and *xz* hopping parameters. **b** Relative change of NN, 2NN, and 3NN $J_{\mathrm{eff}} = 1/2$ overlap normalized by their values in pristine condition (τ_0, τ' and τ'', correspondingly. 2NN and 3NN hoppings for t_{2g} orbitals used to calculate τ's are shown in SI.).

accounting for the change of bond angle θ. This is also consistent with the quantum chemistry study[22].

However, not all trends obtained from the DFT calculations are well reproduced: the hopping parameter $E_{\S\dagger,\S\dagger}$ is increasing under compressive strain (Fig. 3c), unlike the t_1 hopping extracted from DFT (Fig. 2b). To address this, we also consider the O-mediated indirect Ir−O−Ir hoppings.

The indirect oxygen-mediated overlap between the two rotated NN *xy* orbitals can be calculated as a sum of the hopping integrals between two Ir atoms via $\alpha = p_x$, p_y orbitals of the oxygen, $\tilde{E}_{\mathrm{xy,O,xy}} = \sum_{\alpha=p_x,p_y} E_{\mathrm{xy},\alpha,\mathrm{xy}}$. The hopping integral is calculated as

$$\tilde{E}_{\mathrm{xy},\alpha,\mathrm{xy}} = (\cos(2\theta)E^{-l,m,n}_{\alpha,\mathrm{xy}} + \sin(2\theta)E^{-l,m,n}_{\alpha,\mathrm{x^2-y^2}}) \times (\cos(2\theta)E^{l,m,n}_{\alpha,\mathrm{xy}} - \sin(2\theta)E^{l,m,n}_{\alpha,\mathrm{x^2-y^2}})/\Delta_{\mathrm{pd}}, \quad (4)$$

where $l = \cos\theta$, $m = \sin\theta$, $n = 0$ are the directional cosines of the vector from the oxygen O to the Ir atom[43] along the a'-axis in the units of Ir-O distance $d_{\mathrm{Ir-O}} = 0.5d_0^{\mathrm{Ir-Ir}}/\cos\theta$ (d_0^{Ir-Ir} is the distance between the NN Ir ions under ambient conditions), and $E_{\alpha,\mathrm{xy}}$, $E_{\alpha,\mathrm{xy}}$ are the *p-d* Slater-Koster integrals[43]. We note that l, m, n indexes were omitted for Eqs. (1–3), because for the *d*−*d* overlap, Slater-Koster integrals are quadratic in directional cosines[43], and simply $\{l, m, n\} = \{1, 0, 0\}$ for a pair of Ir atoms along the a' bond. For the indirect oxygen-mediated overlap, however, one has to account for the sign of the directional cosines. Moreover, for the indirect hopping, the Ir-O-Ir hopping has to be renormalized by the charge transfer energy $\Delta_{\mathrm{pd}} = E^{\mathrm{on-site}}_{\mathrm{xy}} - E^{\mathrm{on-site}}_{\alpha}$, the energy difference between corresponding Ir-*d* and O-*p* orbitals (see Supplementary Fig. 3a). Surprisingly, the charge transfer energy Δ_{pd} has a strongly non-linear dependency on the strain (see Supplementary Fig. 3a).

We plot the resulting indirect superexchange matrix elements $\tilde{E}$ as a function of the in-plane octahedral rotation θ, Ir-Ir distance d in Fig. 4. Indeed, the indirect Ir-Ir overlap decreases drastically under compressive strain, unlike the direct *d*−*d* overlap. Interestingly, this behavior is directly linked to both the change in the distance between the atoms as well as the angle θ describing octahedra rotation (see Fig. 4a,b). We also note that taking into account the strain dependence of the iridium and oxygen on-site energies is crucial to obtain correct trends. In fact, nonlinear behavior of charge transfer energy Δ_{pd} seems to be directly responsible for the non-linear strain dependency of the indirect oxygen-mediated hopping $\tilde{E}$. This suggests that the role of oxygens in the low-energy physics of strained iridates and other transitional-metal oxides might be underestimated and requires further investigation.

Accordingly, the contribution of the indirect orbital overlap should be small for *xz* and *yz* orbitals. Indeed, the indirect *yz*-*yz* orbitals overlap along a'-axis is zero. The *xz* orbitals hybridize with O-p_z orbital, however, this hybridization decreases with strain much slower than for *xy* orbitals, explaining the different behavior of *xy* and *xz* orbitals under compressive strain.

The fact that relative Ir-O hybridization is directly responsible for the resulting suppression of t_1 (*xy*-*xy* hopping) under compressive strain suggests an electronic state crossover as the role of *xy* orbitals in the composite $J_{\mathrm{eff}} = 1/2$ is decreasing. Notably, a pressure-induced phase transition was also suggested in a recent X-ray powder diffraction study[46] at pressures around 20 GPa, which should correspond to ~−3% strain and is in good agreement with our findings.

Overlap of the spin-orbit coupled J_{eff} states

We now estimate the overlap between the $J_{\mathrm{eff}} = 1/2$ states for NN, 2NN, and 3NN (denoted τ, τ' and τ'', correspondingly), which can be calculated from t_{2g} orbitals overlap using the Clebsh-Gordon coefficients[2,47]. In Fig. 5, we show the change of the overlap of NN $J_{\mathrm{eff}} = 1/2$ states calculated from the DFT values obtained here. As experimental values of $J_{\mathrm{eff}} = 1/2$ states overlap τ are hard to measure, one can try to compare hopping parameters τ with available experimental estimates of magnetic exchange interactions $\mathcal{J}$ (see Table 1 in ref. [23]), which in ambient conditions are assumed to scale with τ^2[22]. However, in a recent RIXS study on strained Sr_2IrO_4[23], the authors suggest that the simple $\mathcal{J} \propto \tau^2/U$ relationship fails for strained Sr_2IrO_4 due to the polaronic renormalization of the charge excitations. In particular, the first-neighbor exchange interaction $\mathcal{J}_1$ was shown to decrease slightly upon the tensile strain, while $\mathcal{J}_2$ and $\mathcal{J}_3$ decreased much faster, based on a fit of the Heisenberg model to the measured magnon dispersion[23]. An earlier RIXS study also suggested that magnetic exchange interaction $\mathcal{J}$ increases upon the compressive strain[22].

Consistent with both RIXS studies[22,23], calculated here values of NN, 2NN, and 3NN hopping parameters are all decreasing upon tensile strain (Fig. 5). As discussed in ref. [23], this trend for τ's is significantly slower than that observed for superexchange interaction $\mathcal{J}$, indicating that $\mathcal{J} \propto \tau^2/U$ relationship indeed fails

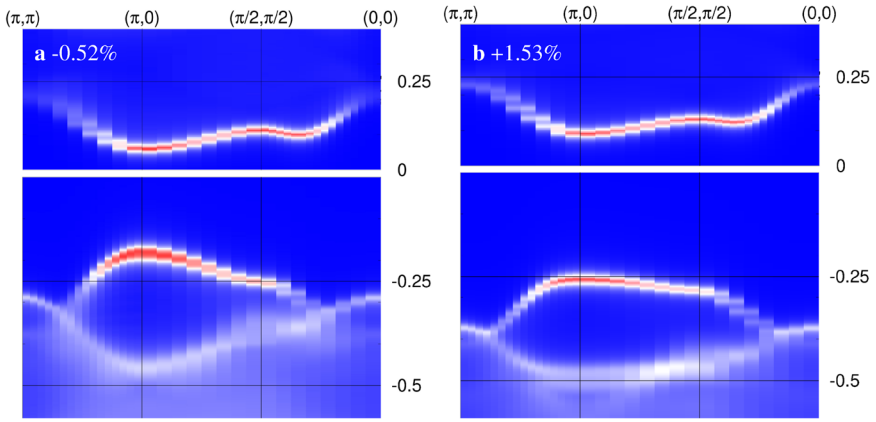

Fig. 5 Dependency of the spectral function of Sr_2IrO_4 on the strain. Spectral function calculated for various strain values: **a** LSAT, −0.52% (compressive strain), **b** GSO, +1.53% (tensile strain) corresponding to ARPES (negative energies) and inversed photoemission spectra (positive energy). The horizontal axis is the 2D crystal momentum. The vertical axis is the energy (eV), where zero energy represents the Fermi level.

for strained Sr_2IrO_4. Our DFT strain trends are also consistent with the modest increase of magnetic exchange interaction $\mathcal{J}_1$ under compressive strain reported in the two-magnon Raman study[24].

It is interesting to compare the trends observed in Sr_2IrO_4 to those in 3*d* transition metal oxides—cuprates. In ref. [48] authors used XAS at Cu L_3-edge of La_2CuO_4 together with analytical and DFT theoretical approaches to show that both bandwidth and electron–electron correlations were increasing upon the compressive strain. As a result, magnetic exchange $\mathcal{J}$ was shown to increase (decrease) almost linearly upon the compressive (tensile) strain. In comparison, while the orbital-dependent hoppings in Sr_2IrO_4 behave very differently from this (Fig. 2b), showing the surprising decrease in t_1 with compressive strain, effective $J_{\text{eff}} = 1/2$ orbitals in Sr_2IrO_4 have strain dependence (Fig. 5) somewhat similar to those of cuprates, echoing the famous parallel between Sr_2IrO_4 and La_2CuO_4.

The evolution of the Fermi surface under strain

Structural response to strain may also be accompanied by changes in the Fermi surface. Thus, strong changes in Fermi surface upon uniaxial pressure have recently been reported in Ru-based compound Sr_2RuO_4[49,50], along with the more than double increase of the superconducting transition temperature[51]. A recent work on Sr_2IrO_4 employing a tight-binding model has pointed out that out-of-plane tilting of the oxygen octahedra can induce shrinking of the Fermi surface and suppress nesting and the *d*-wave superconductivity[52]. There is no out-of-plane tilting in Sr_2IrO_4 under pristine conditions or modest strain—it was very recently shown to appear only under the pressure of as much as 40 GPa[6]. However, in-plane octahedra rotation is strongly affected by the modest strain already, and it is important to understand if and how the Fermi surface is affected, particularly on the beyond-mean-field level.

To study the evolution of the Fermi surface under strain we calculate photoemission spectral functions of strained Sr_2IrO_4, using extended $t-\mathcal{J}$ model formalism developed in ref. [53]. The extended $t-\mathcal{J}$ model used in the calculation (see Methods) depends on two sets of parameters: the magnetic exchange parameters $\mathcal{J}_1$, $\mathcal{J}_2$, $\mathcal{J}_3$, Ising anisotropy coefficient Δ[54], and the hopping parameters t_i describing overlap of the t_{2g} orbitals. We obtain the set of t_i's for each strain value from DFT calculations as discussed in detail above. Using this Wannier Hamiltonian as a starting point describing single-particle hopping processes, we consider all possible many-body hopping processes to derive the hopping part of the extended $t-\mathcal{J}$ model[53].

To properly account for the changes in the electronic structure, we need to account for the evolution of the magnetic exchange parameters with the strain. It has been obtained from the published[23] fits to the RIXS spectra on strained samples. As experimental data is available for small strain values range only, we restrict calculations of photoemission spectra to that range and show the photoemission (and inverse photoemission) spectra in Fig. 6 for two substrates: $(LaAlO_3)_{0.3}(Sr_2AlTaO_6)_{0.7}$ (100) (LSAT) and $GdScO_3$ (110) (GSO), providing a strain of −0.52% and +1.53%, correspondingly.

Calculated photoemission spectra show one conductance band at positive energies, and two valence bands at negative energies: a sharp singlet band around −0.25 eV and a more incoherent triplet band at −0.5 eV. (see Fig. 7 for a detailed discussion on the band character). We see that the strain-induced changes of the photoemission spectra are quite prominent for samples with a strain difference of 2%. First, for tensile strain, as compared to compressive strain, the Mott gap increases (Fig. 6b), suggesting stronger polaron binding of the photoinduced hole to the magnetic background[23]. Second, upon compressive strain, the photoemission spectra of Sr_2IrO_4 show a highly dispersive singlet band (Fig. 6a), while upon tensile strain, both singlet and triplet bands are much less dispersive, and the Fermi surface of Sr_2IrO_4becomes relatively flat (Fig. 6b). It is important to note that the relative flattening of the Fermi sheet upon tensile strain is a many-body effect distinct from the anisotropic compass-like hoppings under compressive strain. One should be able to observe such significant renormalization of the spectral weight in the ARPES data even for small, realistic values of strain.

The conduction band is only weakly affected by strain. Figure 6 shows a marginal flattening of the conduction band upon the tensile strain. We, therefore, expect a minimal effect of epitaxial strain on possible superconductivity.

To explore the effect of strain on the ARPES spectra in more detail, we plot in Fig. 7 separate contributions of the singlet ($J=0$) and triplet ($J=1$) charge excitations to the full spectra. As one can see, under tensile strain, $J=0$ contributes the most at (π,0), whereas under compressive strain, its contribution is slightly more widespread. On the contrary, the $J=1$ spectral weight is shifted to $(\pi/2, \pi/2)$ at the tensile strain and to $(\pi, 0)$ at the compressive strain. In particular, $J=1$ contribution to the "lower energy" band of the photoemission spectra is strongly reduced upon the tensile strain. We thus observe strain-controlled spectral weight redistribution between the charge carriers of singlet and triplet characters. Already moderate tensile strain is sufficient to make the lower energy band of almost purely singlet character.

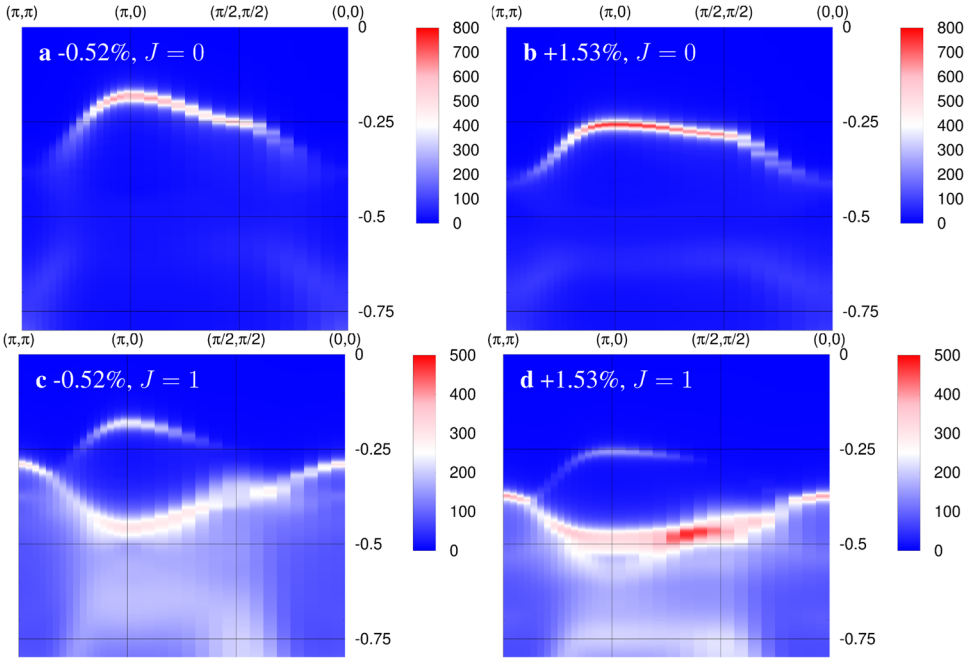

Fig. 6 Contribution of singlet $J = 0$ and triplet $J = 1$ states to the spectral function of Sr_2IrO_4 for various strain values. Singlet $J = 0$ contribution to the ARPES spectral function: **a** LSAT, −0.52% (compressive strain), **b** GSO, +1.53% (tensile strain); Triplet $J = 1$ contribution to the ARPES spectral function: **c** LSAT, −0.52% (compressive strain), **d** GSO, +1.53% (tensile strain). The horizontal axis is the 2D crystal momentum. The vertical axis is the energy (eV), where zero energy represents the Fermi level.

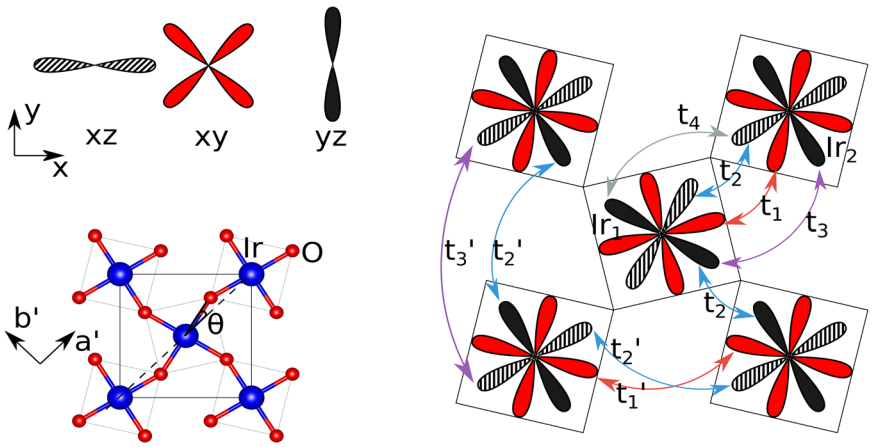

Fig. 7 In-plane structure of Sr_2IrO_4 and the notation for orbital overlap parameters. For nearest neighbors (NN), interorbital overlap parameters are denoted t_1, t_2, t_3, and intraorbital t_4, and for second nearest neighbors (2NN) we consider interorbital overlap only: t', t', t'. Orbital overlap between third neighbors is defined in the same way, not shown. Due to the symmetry considerations, the overlap of out-of-plane t_{2g} orbitals is anisotropic: t_2 describes hopping between $xz(yz)$ along a' (b') axis. The O-Ir-Ir angle θ characterizes the in-plane octahedra rotation as shown.

In summary, we predict a dramatic strain dependence of the electronic properties of Sr_2IrO_4 for compressive v/s tensile strain. The most remarkable feature is the appearance of the compass-model-like contribution of electron propagation due to the separation of the Fermi sea in Sr_2IrO_4 into two subsets of bond- and orbital-dependent carriers under compressive strain. This enables the formation of charge density wave due to nesting and could be connected to the puzzling metalization avoidance in Sr_2IrO_4 upon pressure. The Fermi sea separation originates from strain dependency of relative Ir-O hybridization, as well as on-site O energy, suggesting an important role of oxygens in a low-energy physics of strained iridates and other transitional-metal oxides.

Despite the suppression of the bond-independent xy hopping t_1 under compressive strain, the hopping amplitude of the composite $J_{\text{eff}} = 1/2$ state still increases under compressive strain owing to the contribution from hoppings between xz/yz orbitals (t_2)—the largest of two in-plane nearest-neighbor direction-dependent hoppings. The obtained trends for $J_{\text{eff}} = 1/2$ hopping, τ, are in good agreement with available experimental data.

We also calculated the photoemission spectra of Sr_2IrO_4 upon compressive and tensile strain (for samples grown on LSAT and GSO substrates, respectively). We find that under compressive (tensile) strain, the singlet band becomes significantly more (less) dispersive, and both the singlet and triplet bands shift up (down) in energy. We also show that the electronic properties of the low-energy model can be controlled by strain, since the already moderate tensile strain is sufficient to make the lower energy band of almost purely singlet character, and shift the triplet spectral weight to $(\pi/2, \pi/2)$ point. These features can be readily

observed in the future ARPES measurements—a smoking gun test of our findings.

METHODS

DFT calculations

The DFT results are calculated by the Quantum Espresso package[55] using Perdew-–Burke–Ernzerhof exchange-correlation functional[39] and projector-augmented-wave pseudopotentials[56] with the unit cell containing 16 Sr, 8 Ir, and 32 O atoms. In the calculations of structure relaxation and electronic structure, spin-orbit interaction is not included. The unstrained structure ($a = 5.5098$ Å, $c = 26.1522$ Å) is acquired through relaxing both the lattice geometry and the atomic positions. For biaxial-strained structures, the *a*- and *b*-axis are fixed as per the strain value while the *c*-axis and the atomic positions are simultaneously relaxed. The plane wave cutoff energy is set to be 40 Ry, and a Γ-centered $10 \times 10 \times 2k$-points in the full Brillouin zone are sampled. The structural and electronic convergence criteria were set to be 10^{-4} Ry/a_0 and 10^{-6} Ry, respectively.

With the DFT eigenvalues and eigenvectors, we then use Wannier90 package[57] and implement a disentanglement procedure to obtain the Wannier functions and the hopping parameters. During the disentanglement, 120 bands were considered, which accounted for contributions from 96 (32×3) O-2*p* orbitals and 24 (8×3) Ir-t_{2g} orbitals. Four iridium layers (i.e., 8 Ir atoms) are involved to construct 24 wannierized t_{2g} orbitals in one unit cell (6 Wannier functions per Ir layer).

Calculation of the photoemission spectra

The ARPES spectral function is obtained as imaginary part of the Green function $G(\mathbf{k}, \omega)$ describing propagation of the photohole in the ground state, dressed in the low-energy magnetic excitations (magnons): $G(\mathbf{k}, \omega) = \mathrm{Tr}\langle \mathrm{AF}|\mathbf{h}_{\mathbf{k}} \frac{1}{\omega - \mathcal{H}_{t-\mathcal{J}} + i\delta} \mathbf{h}_{\mathbf{k}}^{\dagger}|\mathrm{AF}\rangle$. Here, photohole $\mathbf{h}_{\mathbf{k}}$ is a vector in a full spin-orbital Hilbert space, obtained by projecting three t_{2g} orbitals of Ir atom onto the spin-orbit coupled basis[53,58]. The motion of the hole is governed by $t - \mathcal{J}$ Hamiltonian $\mathcal{H}_{t-\mathcal{J}} = \mathcal{H}_t + \mathcal{H}_{\mathcal{J}}$. The magnetic $H_{\mathcal{J}}$ part includes NN, 2NN, and 3NN Heisenberg interactions $\mathcal{J}_1$, $\mathcal{J}_2$, $\mathcal{J}_3$ and an anisotropic Δ term, arising from non-negligible Hund's coupling[54,59]:

$$\begin{aligned}\mathcal{H}_{\mathcal{J}} = \mathcal{J}_1 \sum_{\langle i,j \rangle} \left(\tilde{\mathbf{S}}_i^x \tilde{\mathbf{S}}_j^x + \tilde{\mathbf{S}}_i^y \tilde{\mathbf{S}}_j^y + (1-\Delta) \tilde{\mathbf{S}}_i^z \tilde{\mathbf{S}}_j^z \right) \\ + \mathcal{J}_2 \sum_{\langle\langle i,j \rangle\rangle} \tilde{\mathbf{S}}_i \cdot \tilde{\mathbf{S}}_j + \mathcal{J}_3 \sum_{\langle\langle\langle i,j \rangle\rangle\rangle} \tilde{\mathbf{S}}_i \cdot \tilde{\mathbf{S}}_j\end{aligned} \quad (5)$$

The hopping $\mathcal{H}_t$ part is derived by projecting multiorbital Hubbard model employing orbital-dependent hopping parameters t_i onto spin-orbit coupled basis[53,58]. The motion of a charge excitation in the new spin-orbit coupled basis is then expressed analytically in terms of these t_i which are obtained directly from DFT[53,58]. We evaluate the Green function $G(\mathbf{k}, \omega)$ using the SCBA[60]. SCBA is a diagrammatic approach that evaluates Green function of a quasiparticle dressed with bosons (here, photohole dressed with magnons) that form diagrams of rainbow type[60]. The spectral functions are calculated numerically for a 16×16 cluster.

DATA AVAILABILITY

All the data that support the findings of this study are available from the corresponding author (E.M.P.) upon reasonable request.

CODE AVAILABILITY

The codes used in this study are available from the corresponding author (E.M.P.) on reasonable request.

Received: 13 October 2021; Accepted: 16 August 2022;
Published online: 10 September 2022

REFERENCES

1. Kim, B. J. et al. Novel $J_{\mathrm{eff}} = 1/2$ Mott state induced by relativistic spin-orbit coupling in Sr_2IrO_4. *Phys. Rev. Lett.* **101**, 076402 (2008).
2. Jackeli, G. & Khaliullin, G. Mott insulators in the strong spin-orbit coupling limit: from Heisenberg to a quantum compass and Kitaev models. *Phys. Rev. Lett.* **102**, 017205 (2009).
3. Cao, G. & Schlottmann, P. The challenge of spin–orbit-tuned ground states in iridates: a key issues review. *Rep. Prog. Phys.* **81**, 042502 (2018).
4. Snow, C. S. et al. Pressure-tuned collapse of the Mott-like state in $Ca_{n+1}Ru_nO_{3n+1}$ ($n = 1, 2$): Raman spectroscopic studies. *Phys. Rev. Lett.* **89**, 226401 (2002).
5. Haskel, D. et al. Pressure tuning of the spin-orbit coupled ground state in Sr_2IrO_4. *Phys. Rev. Lett.* **109**, 027204 (2012).
6. Chen, C. et al. Persistent insulating state at megabar pressures in strongly spin-orbit coupled Sr_2IrO_4. *Phys. Rev. B* **101**, 144102 (2020).
7. Ding, Y. et al. Pressure-induced confined metal from the Mott insulator $Sr_3Ir_2O_7$. *Phys. Rev. Lett.* **116**, 216402 (2016).
8. Zhang, J. et al. Lattice frustration in spin-orbit Mott insulator $Sr_3Ir_2O_7$ at high pressure. *npj Quantum Mater.* **4**, 23 (2019).
9. Korneta, O. B. et al. Pressure-induced insulating state in $Ba_{1-x}R_xIrO_3$ (R = Gd, Eu) single crystals. *Phys. Rev. B* **81**, 045101 (2010).
10. Cao, G., Bolivar, J., McCall, S., Crow, J. E. & Guertin, R. P. Weak ferromagnetism, metal-to-nonmetal transition, and negative differential resistivity in single-crystal Sr_2IrO_4. *Phys. Rev. B* **57**, R11039–R11042 (1998).
11. Haskel, D. et al. Possible quantum paramagnetism in compressed Sr_2IrO_4. *Phys. Rev. Lett.* **124**, 067201 (2020).
12. Rayan Serrao, C. et al. Epitaxy-distorted spin-orbit Mott insulator in Sr_2IrO_4 thin films. *Phys. Rev. B* **87**, 085121 (2013).
13. Nichols, J. et al. Emerging magnetism and anomalous Hall effect in iridate-manganite heterostructures. *Nat. Commun.* **7**, 12721 (2016).
14. Yi, D. et al. Atomic-scale control of magnetic anisotropy via novel spin–orbit coupling effect in $La_{2/3}Sr_{1/3}MnO_3/SrIrO_3$ superlattices. *Proc. Natl Acad. Sci.* **113**, 6397–6402 (2016).
15. Okamoto, S. et al. Charge transfer in iridate-manganite superlattices. *Nano Lett.* **17**, 2126–2130 (2017).
16. Gruenewald, J. H. et al. Engineering 1D quantum stripes from superlattices of 2D layered materials. *Adv. Mater.* **29**, 1603798 (2017).
17. Kim, J.-W. et al. Controlling entangled spin-orbit coupling of 5*d* states with interfacial heterostructure engineering. *Phys. Rev. B* **97**, 094426 (2018).
18. Wen, F. et al. Interface-engineered hole doping in $Sr_2IrO_4/LaNiO_3$ heterostructure. *N. J. Phys.* **21**, 103009 (2019).
19. Meyers, D. et al. Magnetism in iridate heterostructures leveraged by structural distortions. *Sci. Rep.* **9**, 4263 (2019).
20. Dasa, T. R., Hao, L., Liu, J. & Xu, H. Designing iridate-based superlattice with large magnetoelectric coupling. *J. Mater. Chem. C.* **7**, 13294–13300 (2019).
21. Mohanta, N., Dagotto, E. & Okamoto, S. Topological Hall effect and emergent skyrmion crystal at manganite-iridate oxide interfaces. *Phys. Rev. B* **100**, 064429 (2019).
22. Lupascu, A. et al. Tuning magnetic coupling in Sr_2IrO_4 thin films with epitaxial strain. *Phys. Rev. Lett.* **112**, 147201 (2014).
23. Paris, E. et al. Strain engineering of the charge and spin-orbital interactions in Sr_2IrO_4. *Proc. Natl Acad. Sci.* **117**, 24764–24770 (2020).
24. Seo, A. et al. Compressive strain-induced enhancement of exchange interaction and short-range magnetic order in Sr_2IrO_4 investigated by Raman spectroscopy. *Phys. Rev. B* **100**, 165106 (2019).
25. Souri, M. et al. Crossover between Mott and Efros-Shklovskii variable-range hopping in Sr_2IrO_4 epitaxial thin films by misfit strain and isovalent doping. *J. Appl. Phys.* **126**, 185101 (2019).
26. Cuk, T. et al. Uncovering a pressure-tuned electronic transition in $Bi_{1.98}Sr_{2.06}Y_{0.68}Cu_2O_{8+\delta}$ using Raman scattering and X-Ray diffraction. *Phys. Rev. Lett.* **100**, 217003 (2008).
27. Cao, G. et al. Electrical control of structural and physical properties via strong spin-orbit interactions in Sr_2IrO_4. *Phys. Rev. Lett.* **120**, 017201 (2018).
28. Ye, F., Hoffmann, C., Tian, W., Zhao, H. & Cao, G. Pseudospin-lattice coupling and electric control of the square-lattice iridate Sr_2IrO_4. *Phys. Rev. B* **102**, 115120 (2020).
29. Son, J. et al. Unconventional spin-phonon coupling via the Dzyaloshinskii-Moriya interaction. *npj Quantum Mater.* **4**, 17 (2019).
30. Dashwood, C. D. et al. Momentum-resolved lattice dynamics of parent and electron-doped Sr_2IrO_4. *Phys. Rev. B* **100**, 085131 (2019).
31. Liu, H. & Khaliullin, G. Pseudo-Jahn-Teller effect and magnetoelastic coupling in spin-orbit Mott insulators. *Phys. Rev. Lett.* **122**, 057203 (2019).
32. Samanta, K., Rigitano, D., Pagliuso, P. G. & Granado, E. Isospin-phonon coupling and Fano-interference in spin-orbit Mott insulator Sr_2IrO_4. *Appl. Phys. Lett.* **114**, 152402 (2019).
33. Nichols, J. et al. Tuning electronic structure via epitaxial strain in Sr_2IrO_4 thin films. *Appl. Phys. Lett.* **102**, 141908 (2013).
34. Bhandari, C., Popović, Z. S. & Satpathy, S. Electronic structure and optical properties of Sr_2IrO_4 under epitaxial strain. *N. J. Phys.* **21**, 013036 (2019).
35. Zaitsev, A. G. et al. Anomalous pressure dependence of the electronic transport and anisotropy in $SrIrO_3$ films. *J. Phys. Condens. Matter* **32**, 345601 (2020).

36. Choi, S. et al. Lattice dynamics and structural transition of the hyperhoneycomb iridate $\beta - Li_2IrO_3$ investigated by high-pressure Raman scattering. *Phys. Rev. B* **101**, 054102 (2020).
37. Engström, L., Pereg-Barnea, T. & Witczak-Krempa, W. Modeling multiorbital effects in Sr_2IrO_4 under strain and a Zeeman field. *Phys. Rev. B* **103**, 155147 (2021).
38. Nicholson, C. W. et al. Uniaxial strain-induced phase transition in the 2D topological semimetal $IrTe_2$ films. *Commun. Mater.* **2**, 25 (2021).
39. Perdew, J. P., Burke, K. & Ernzerhof, M. Generalized gradient approximation made simple. *Phys. Rev. Lett.* **77**, 3865–3868 (1996).
40. Boseggia, S. et al. Locking of iridium magnetic moments to the correlated rotation of oxygen octahedra in Sr_2IrO_4 revealed by x-ray resonant scattering. *J. Phys. Condens. Matter* **25**, 422202 (2013).
41. Nussinov, Z. & van den Brink, J. Compass models: theory and physical motivations. *Rev. Mod. Phys.* **87**, 1–59 (2015).
42. Glazer, A. M. The classification of tilted octahedra in perovskites. *Acta Crystallogr. Sect. B* **28**, 3384–3392 (1972).
43. Harrison, W. A. *Elementary Electronic Structure* (World Scientific Press, Singapore, 2004).
44. Slater, J. C. & Koster, G. F. Simplified LCAO method for the periodic potential problem. *Phys. Rev.* **94**, 1498–1524 (1954).
45. Wang, F. & Senthil, T. Twisted Hubbard model for Sr_2IrO_4: Magnetism and possible high-temperature superconductivity. *Phys. Rev. Lett.* **106**, 136402 (2011).
46. Samanta, K., Tartaglia, R., Kaneko, U. F., Souza-Neto, N. M. & Granado, E. Anisotropic lattice compression and pressure-induced electronic phase transitions in Sr_2IrO_4. *Phys. Rev. B* **101**, 075121 (2020).
47. Plotnikova, E. M., Daghofer, M., van den Brink, J. & Wohlfeld, K. Jahn-Teller effect in systems with strong on-site spin-orbit coupling. *Phys. Rev. Lett.* **116**, 106401 (2016).
48. Ivashko, O. et al. Strain-engineering Mott-insulating La_2CuO_4. *Nat. Commun.* **10**, 786 (2019).
49. Sunko, V. et al. Direct observation of a uniaxial stress-driven Lifshitz transition in Sr_2RuO_4. *npj Quantum Mater.* **4**, 46 (2019).
50. Barber, M. E. et al. Role of correlations in determining the Van Hove strain in Sr_2RuO_4. *Phys. Rev. B* **100**, 245139 (2019).
51. Taniguchi, H., Nishimura, K., Goh, S. K., Yonezawa, S. & Maeno, Y. Higher-T_c superconducting phase in Sr_2RuO_4 induced by in-plane uniaxial pressure. *J. Phys. Soc. Jpn.* **84**, 14707 (2015).
52. Lindquist, A. W. & Kee, H.-Y. Odd-parity superconductivity driven by octahedra rotations in iridium oxides. *Phys. Rev. B* **100**, 054512 (2019).
53. Pärschke, E. M., Wohlfeld, K., Foyevtsova, K. & van den Brink, J. Correlation induced electron-hole asymmetry in quasi- two-dimensional iridates. *Nat. Commun.* **8**, 686 (2017).
54. Vale, J. G. et al. Importance of *XY* anisotropy in Sr_2IrO_4 revealed by magnetic critical scattering experiments. *Phys. Rev. B* **92**, 020406 (2015).
55. Giannozzi, P. et al. QUANTUM ESPRESSO: a modular and open-source software project for quantum simulations of materials. *J. Phys. Condens. Matter* **21**, 395502 (2009).
56. Blöchl, P. E. Projector augmented-wave method. *Phys. Rev. B* **50**, 17953–17979 (1994).
57. Mostofi, A. A. et al. wannier90: a tool for obtaining maximally-localised wannier functions. *Comput. Phys. Commun.* **178**, 685–699 (2008).
58. Pärschke, E. M. & Ray, R. Influence of the multiplet structure on the photoemission spectra of spin-orbit driven Mott insulators: application to Sr_2IrO_4. *Phys. Rev. B* **98**, 064422 (2018).
59. Pincini, D. et al. Anisotropic exchange and spin-wave damping in pure and electron-doped Sr_2IrO_4. *Phys. Rev. B* **96**, 075162 (2017).
60. Martinez, G. & Horsch, P. Spin polarons in the t-J model. *Phys. Rev. B* **44**, 317–331 (1991).

ACKNOWLEDGEMENTS

E.M.P. thanks Eugenio Paris, Thorsten Schmitt, Krzysztof Wohlfeld, and other coauthors for an inspiring previous collaboration[23], and is grateful to Gang Cao, Ambrose Seo, and Jungho Kim for insightful discussions. R.R. acknowledges helpful discussion with Sanjeev Kumar and Manuel Richter. This project has received funding from the European Union's Horizon 2020 research and innovation program under the Marie Sklodowska-Curie grant agreement No 754411. C.C.C. acknowledges support from the U.S. National Science Foundation Award No. DMR-2142801.

AUTHOR CONTRIBUTIONS

E.M.P. designed the project and carried out the photoemission spectra calculations. E.M.P. and R.R. performed the Slater-Koster analysis. W.C.C. carried out the DFT and Wannier function analysis. E.M.P. and C.C.C. supervised the project. All the authors analyzed the results. E.M.P. wrote the manuscript with the help of R.R. and C.C.C.

COMPETING INTERESTS

The authors declare that there are no competing interests.

ADDITIONAL INFORMATION

Supplementary information The online version contains supplementary material available at https://doi.org/10.1038/s41535-022-00496-w.

Correspondence and requests for materials should be addressed to Ekaterina M. Pärschke.

Reprints and permission information is available at http://www.nature.com/reprints

Publisher's note Springer Nature remains neutral with regard to jurisdictional claims in published maps and institutional affiliations.